

Cluster-Adaptive Sample-Based Quantum Diagonalization for Strongly Correlated Systems

Byeongyong Park¹, Sanha Kang¹, Jongseok Seo¹, Juhee Baek²,
Doyeol (David) Ahn^{1,3}, Keunhong Jeong^{2*}

¹Center for Quantum Information Processing, University of Seoul, 163
Seoulsiripdae-Ro, Dongdaemun-Gu, Seoul, 02504, Republic of Korea.

²Department of Chemistry, Sogang University, 35 Baekbeom-ro, Mapo-gu, Seoul,
04107, Republic of Korea.

³Singularity Quantum Inc, 9506 Villa Isle Drive, Villa Park, CA, 92861, USA.

*Corresponding author(s). E-mail(s): doas1mind@sogang.ac.kr;
Contributing authors: by7816@uos.ac.kr; sanha9156@uos.ac.kr;
sjs981212@uos.ac.kr; bjhee1116@gmail.com; dahn@uos.ac.kr;

Abstract

Strongly correlated electronic systems exhibit inherently multiconfigurational wave functions, making it difficult to construct compact variational subspaces that preserve the essential multireference character. Quantum computing has emerged as a promising route to alleviate these limitations, and sample-based quantum diagonalization (SQD) is a representative hybrid approach that uses quantum hardware as a determinant sampler followed by classical diagonalization in the projected subspace. To mitigate hardware noise, SQD employs a self-consistent particle-number recovery guided by a single global reference occupancy vector. However, in strongly correlated, multimodal regimes, this global reference can become mixture-averaged and bias recovery toward a mean pattern, diluting mode-specific occupation structure and degrading the determinant pool. Here, we introduce cluster-adaptive SQD (CSQD), which clusters measurement samples via unsupervised learning and performs particle-number recovery using cluster-specific, self-consistently updated reference occupancy vectors. Under a matched variational budget, we benchmarked CSQD against SQD for N₂ dissociation in a (10e,26o) active space and the [2Fe–2S] cluster in a (30e,20o) active space. Our results indicate that CSQD offers an advantage over SQD in estimating the ground-state energy in the strongly correlated regime, lowering the variational estimate by up to 15.95 mHa for stretched N₂ and up to 45.53 mHa for [2Fe–2S], with modest additional classical overhead.

1 Introduction

Understanding strongly correlated electronic systems, such as transition-metal oxides [1], high-temperature superconductors [2], and multiradical species [3, 4], remains a central challenge in modern quantum chemistry and condensed matter physics [5–9]. A characteristic feature of these systems is that the electron–electron Coulomb interaction competes with or even dominates the kinetic energy. This competition induces a dense set of near-degenerate many-electron states, rendering the electronic structure intrinsically multiconfigurational [8–10]. Crucially, chemically important information is frequently encoded in determinants that are weakly connected to the dominant configurations or reside within the low-weight tails of the wave function distribution.

Consequently, methodologies based on the single-reference approximation, including Hartree–Fock (HF), coupled-cluster theory, and density functional theory (DFT), often fail qualitatively to capture the essential physics of these systems [11–13].

To address strongly correlated systems, full configuration interaction (FCI), which treats the entire Hilbert space exactly, is limited by the combinatorial growth of the state space, with reported demonstrations reaching system sizes of 22 electrons in 22 orbitals (22e,22o) [14] and 26 electrons in 23 orbitals (26e,23o) [15]. As an efficient alternative, selected configuration interaction (SCI) algorithms [16–19], notably heat-bath configuration interaction (HCI) [18, 19], exploit the inherent sparsity of the wave function. These methods iteratively expand the variational space by considering Hamiltonian-connected external determinants and selecting those whose estimated contributions exceed a prescribed cutoff. However, this local expansion implicitly assumes that chemically important configurations are reachable through successive additions, requiring intermediate determinants to be sufficiently important to be selected. In strongly correlated systems where the wave function is multiconfigurational, this assumption can become less reliable. When important configurations are separated by chains of intermediate determinants with negligible weights, classical selection heuristics may require much tighter cutoffs to recover them and may otherwise yield suboptimal variational spaces [20–22].

Quantum SCI (QSCI) methods offer the potential to overcome the locality limitations of classical SCI, leveraging superposition and interference to explore the Hilbert space more globally [23–35]. In these approaches, the quantum processor serves as a sampler to identify chemically important determinants, before delegating Hamiltonian projection and diagonalization to classical computation. Among QSCI workflows, sample-based quantum diagonalization (SQD) [26] has rapidly emerged as a promising framework. A core feature of SQD is its symmetry-recovery step, which restores particle-number symmetry in noisy samples using a self-consistently updated reference occupancy vector. Recent demonstrations [26, 27] on iron–sulfur (Fe–S) clusters using up to 77 qubits have provided evidence for the feasibility of this strategy in the noisy intermediate-scale quantum (NISQ) [36] era. The SQD protocol is evolving into a broader paradigm for hybrid quantum–classical computing, including extensions such as extended SQD (Ext-SQD) [28] for excited states and sample-based Krylov quantum diagonalization (SKQD) [29] based on time-evolved Krylov-state sampling, as well as combinations with complementary techniques such as quantum embedding [31] and phaseless auxiliary-field quantum Monte Carlo (ph-AFQMC) [30].

However, an important practical consideration in applying SQD to strongly correlated systems is its reliance on a global reference occupancy vector for particle-number recovery. Since the wave function in these systems is typically multiconfigurational, the resulting distribution of electronic configurations is often multimodal. In this case, the global reference occupancy vector becomes a mode-weighted average and may fail to capture the occupancy patterns of specific modes, particularly low-weight yet chemically relevant ones. Particle-number recovery based on this average biases the corrected samples toward a global-mean pattern, diluting mode-specific occupation structure and degrading the determinant pool used for projected diagonalization.

In this work, we propose cluster-adaptive SQD (CSQD), which modifies SQD to mitigate reference bias that can arise from global averaging in its particle-number recovery step in multimodal, strongly correlated regimes. CSQD employs unsupervised learning to cluster quantum samples and uses cluster-specific, self-consistently updated reference occupancy vectors to restore particle-number symmetry within each cluster. By aligning the symmetry recovery with the multimodal character of strongly correlated wave functions, CSQD mitigates recovery bias and yields higher-quality variational subspaces from noisy quantum samples, while incurring only modest classical post-processing overhead.

We benchmarked CSQD against SQD by comparing variational ground-state energy estimates for two representative problems: the dissociation of N_2 in a (10e,26o) active space and the strongly multireference [2Fe–2S] cluster [37] in a (30e,20o) active space. For each benchmark instance, we provided both algorithms with identical quantum samples as input and evaluated them under a matched variational budget, so that performance differences reflected only classical post-processing and subspace construction. For N_2 , SQD often yielded slightly lower variational energies in the weakly correlated regime by at most a few millihartree, whereas in the stretched-bond, strongly correlated regime CSQD yielded lower variational energies in all but one tested setting, with

improvements of up to 15.95 mHa relative to SQD. For [2Fe–2S], CSQD attained lower variational energies than SQD across all tested settings, with energy reductions reaching up to 45.53 mHa at the largest matched dimension considered. These gains were achieved with only modest additional classical post-processing cost, and reference-occupancy diagnostics supported the interpretation that preserving multimodal structure contributed to the observed improvements in strongly correlated regimes.

2 Results

In this section, we benchmark CSQD against SQD by comparing variational ground-state energy estimates for two representative electronic-structure problems: the dissociation of N_2 and the [2Fe–2S] cluster [37]. For each case, CSQD and SQD are applied to the same set of quantum samples. Since the energy obtained by diagonalizing the projected Hamiltonian is variational, a lower energy at matched final subspace dimension, $\dim(\mathcal{V})$, indicates a higher-quality determinant pool and subspace.

This section is structured as follows: we introduce common notation for determinant-based subspace projection and diagonalization, and provide a conceptual overview of CSQD. Next, we use N_2 as a controlled benchmark spanning weak to strong correlation. We then study [2Fe–2S] as a challenging multireference system, and use reference-occupancy diagnostics to characterize how the learned reference vectors differ between SQD and CSQD and how this correlates with the observed energy improvements. To keep this section focused on benchmark outcomes and their interpretation, we report only the algorithmic and experimental details necessary for clarity, while deferring precise algorithm definitions, complete hyperparameters, and experimental settings to the Methods section.

2.1 Problem Setup and Notation

We consider the electronic-structure problem in a finite basis of spatial orbitals under the Born–Oppenheimer approximation. Our goal is to estimate the ground-state energy and the corresponding wave function of the electronic Hamiltonian. In second quantization, the Hamiltonian is given by

$$\hat{H} = \sum_{pr,\sigma} h_{pr} \hat{a}_{p\sigma}^\dagger \hat{a}_{r\sigma} + \frac{1}{2} \sum_{prqs,\sigma\tau} (pr|qs) \hat{a}_{p\sigma}^\dagger \hat{a}_{q\tau}^\dagger \hat{a}_{s\tau} \hat{a}_{r\sigma}, \quad (1)$$

where p, r, q, s label spatial orbitals, $\sigma, \tau \in \{\alpha, \beta\}$ label spin, and h_{pr} and $(pr|qs)$ denote the one- and two-electron integrals. The operators $\hat{a}_{p\sigma}^\dagger$ and $\hat{a}_{p\sigma}$ are the fermionic creation and annihilation operators for the spin orbital (p, σ) . The Hamiltonian conserves the numbers of α and β electrons; accordingly, we work in a fixed particle-number sector (N_α, N_β) . Throughout this work, we restrict to the $S_z = 0$ sector with $N_\alpha = N_\beta \equiv N_\sigma$.

We map the fermionic degrees of freedom to qubits using a Jordan–Wigner transformation [38], in which each qubit encodes the occupancy of a spin orbital and computational-basis measurements return bitstrings $x \in \{0, 1\}^{2N_{\text{MO}}}$, where N_{MO} is the number of spatial orbitals. Each bitstring corresponds to a Slater determinant,

$$|x\rangle = \prod_{p\sigma} (\hat{a}_{p\sigma}^\dagger)^{x_{p\sigma}} |\text{vac}\rangle, \quad (2)$$

where the product is taken in a fixed canonical order of spin orbitals and $|\text{vac}\rangle$ represents the vacuum state. Subspace diagonalization approximates the ground state by projecting \hat{H} onto a finite variational subspace \mathcal{V} spanned by a selected set of determinants, and diagonalizing the resulting matrix to obtain a variational energy estimate. In the following, we use quantum sampling to identify chemically important determinants and to construct compact subspaces for projection and diagonalization on a classical computer.

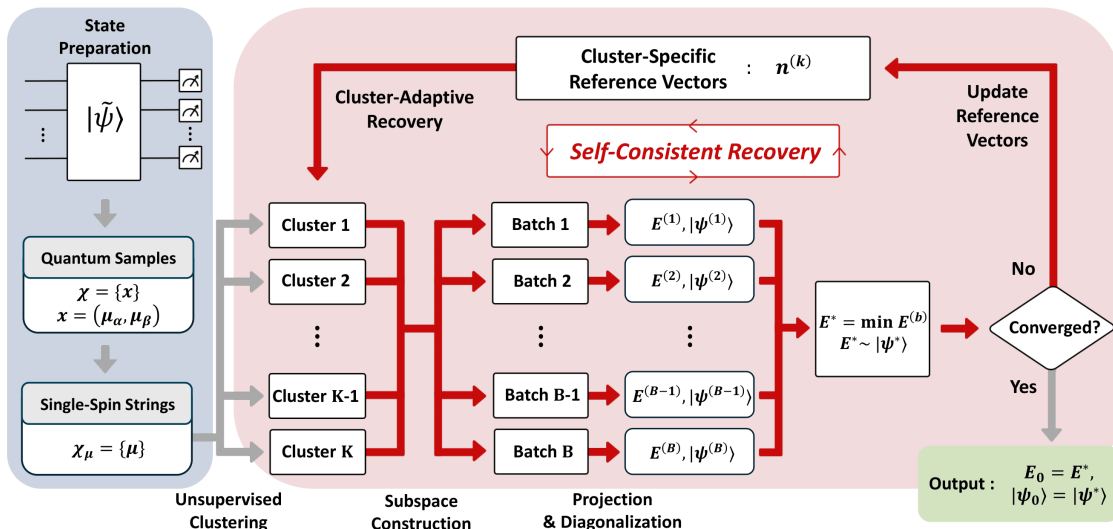


Fig. 1 CSQD workflow for ground-state energy estimation. The left (blue) block shows quantum sampling and preprocessing: a parameterized quantum state $|\tilde{\psi}\rangle$ is prepared and measured repeatedly to collect bitstring samples $x = (\mu_\alpha, \mu_\beta)$, whose spin strings are pooled into single-spin strings $\mathcal{X}_\mu = \{\mu\}$. These strings are partitioned into K clusters via unsupervised clustering. The right (red) block depicts the self-consistent recovery loop for CSQD: for each cluster k , a cluster-specific reference occupancy vector $\mathbf{n}^{(k)}$ guides particle-number recovery. Recovered strings are subsampled into B batches, each defining a determinant subspace. For each batch b , the Hamiltonian projected into the corresponding subspace is constructed and diagonalized to obtain the lowest-energy eigenpair $(E^{(b)}, |\psi^{(b)}\rangle)$. The best batch $b^* = \arg \min_b E^{(b)}$ is selected, $\{\mathbf{n}^{(k)}\}_{k=1}^K$ is updated from $|\psi^{(b^*)}\rangle$, and the recovery–diagonalization loop is iterated until a stopping criterion is met, yielding final estimates $(E_0, |\psi_0\rangle)$.

2.2 Overview of CSQD

CSQD is a variant of SQD that performs particle-number symmetry recovery using cluster-specific reference occupancy vectors, mitigating the bias of a single global reference under multimodal determinant distributions. Fig. 1 provides an overview of the CSQD workflow.

Starting from computational-basis measurements obtained from a single ansatz instance per molecular geometry, we split each sampled bitstring into its α - and β -spin components. These single-spin strings are pooled into a common dataset and partitioned into K clusters via unsupervised learning, such as k -modes [39, 40] or Bernoulli mixture models (BMM) [41, 42], using empirical frequencies as sample weights. This clustering allows us to define a cluster-specific reference occupancy vector $\mathbf{n}^{(k)}$ for each cluster $k \in \{1, \dots, K\}$. Each $\mathbf{n}^{(k)}$ then guides particle-number symmetry recovery within cluster k .

Next, we form a shared pool of single-spin strings with the correct particle number—either intrinsically valid from the initial measurements or corrected via recovery in subsequent iterations—by drawing a total of S samples from the clusters, allocated proportionally to their statistical weights. After deduplication, this pool is truncated to a maximum of d_{\max} strings. To mitigate spin contamination arising from a determinant set that is not closed under spin inversion, we construct a spin-symmetric projected subspace by using this shared pool for both the α and β sectors, analogous to Ref. [26]. The determinant basis is then formed as the tensor product of this pool, yielding a projected subspace of dimension up to d_{\max}^2 . We project the Hamiltonian \hat{H} into this subspace and diagonalize it to obtain a variational ground-state estimate. To reduce stochastic variability from the subsampling process, subspace construction and projected diagonalization are repeated over B independent batches, retaining the ground-state solution that yields the lowest energy.

The cluster-specific reference vectors $\{\mathbf{n}^{(k)}\}$ are then updated from the newly estimated ground-state wave function by aggregating squared determinant amplitudes associated with each cluster. Using these updated $\{\mathbf{n}^{(k)}\}$ vectors, we perform particle-number symmetry recovery on the initial measurement samples, locally correcting particle-number-inconsistent single-spin strings within each associated cluster. To stabilize the subspace across iterations, dominant single-spin strings

are carried over. This entire self-consistent cycle—subspace construction, diagonalization, reference vector update, and recovery—is iterated until the energy and the reference vectors converge, or for at most T iterations.

2.3 Dissociation of N_2 : From Weak to Strong Correlation

The dissociation of N_2 is a standard benchmark that spans the weakly correlated regime near equilibrium (dominated by dynamical correlation) and the strongly correlated regime upon bond stretching (dominated by static correlation), thereby providing a comprehensive test of the proposed CSQD workflow.

We studied N_2 in a frozen-core cc-pVDZ basis with an active space of (10e,26o), scanning bond lengths from $R = 0.7$ to 3.4 \AA in 0.1 \AA steps. The equilibrium bond length is $R_e \approx 1.098 \text{ \AA}$, and we define the strongly correlated regime as $R \geq 1.5R_e \approx 1.647 \text{ \AA}$. Quantum measurement samples were generated following the SQD protocol of Ref. [26]. Experiments were performed on the IBM Heron r2 `ibm_fez` processor. For each geometry, we collected 3×10^5 shots, leaving $\sim 1.08 \times 10^5$ valid outcomes on average after reset-mitigation filtering. Details of the quantum circuit construction, device execution, and error mitigation are provided in Methods.

Using the same filtered measurement outcomes as input to both SQD and CSQD, we swept the target projected-subspace size $\dim(\mathcal{V}) = d_{\text{max}}^2$ with $d_{\text{max}} \in \{1000, 1500, 2000\}$. For CSQD, we swept the clustering model (BMM or k -modes) and the number of clusters $K \in \{2, 3, 4, 5\}$. CSQD and SQD were run for at most 10 and 11 self-consistent iterations, respectively, using $B = 10$ independent batches per iteration and retaining the lowest energy observed across all batches and iterations. SQD was granted one additional iteration because its stricter particle-number postselection in the initial subspace construction often yielded a smaller starting pool and hence a smaller initial $\dim(\mathcal{V})$ than CSQD. In each iteration and batch for both methods, we drew sufficiently many candidate strings such that, after merging newly sampled and carry-over strings and removing duplicates, the single-spin pool in each spin sector was capped at, and typically reached, d_{max} unique strings. This kept the intermediate projected-subspace size close to d_{max}^2 throughout the self-consistent loop, ensuring a comparable variational budget for SQD and CSQD. All classical post-processing was performed as single-node jobs on identical CPU resources (56-core Intel Xeon Gold 6348R with 1 TB RAM).

In the main text, we report results for our largest projected-subspace setting, $d_{\text{max}} = 2000$, corresponding to a final projected-subspace dimension of $\dim(\mathcal{V}) = 4 \times 10^6$. The full set of results for smaller d_{max} is provided in the Supplementary Information.

Fig. 2 visualizes the N_2 dissociation benchmark and highlights the regime-dependent behavior of CSQD for a representative setting ($\dim(\mathcal{V}) = 4 \times 10^6$, BMM, $K = 5$). BMM is a natural choice because it models binary occupation features through a Bernoulli likelihood. For visualization, we use $K = 5$, the largest value considered, as a conservative setting that mitigates potential under-clustering.

In Fig. 2a, HCI provides a high-accuracy classical benchmark for this active space across both the near-equilibrium and stretched-bond regimes. Restricted HF (RHF) and coupled-cluster singles and doubles (CCSD) are shown as single-reference baselines: they are accurate near equilibrium but deteriorate upon bond stretching as static correlation becomes increasingly important. We note that CCSD is not variational and can therefore fall below the benchmark curve in strongly correlated regimes. Both SQD and CSQD closely track the benchmark trend, while CSQD tends to remain closer in the stretched-bond region where single-reference descriptions become inadequate.

Fig. 2b makes the SQD–CSQD comparison explicit. The upper panel plots $\Delta E \equiv E_{\text{CSQD}} - E_{\text{SQD}}$, showing a crossover from the near-equilibrium region, where SQD is often slightly lower, to the stretched-bond region, where CSQD yields consistently lower variational energies. The lower panel reports the RHF weight $|c_{\text{RHF}}|^2$ extracted from the HCI wave function, which generally decreases with bond length and serves as an indicator of the breakdown of a single-reference approximation. As $|c_{\text{RHF}}|^2$ decreases, ΔE tends to become negative, indicating that CSQD tends to outperform SQD as the system enters the strongly correlated regime. This behavior is consistent with the interpretation that cluster-resolved reference occupations can provide a more effective guide for particle-number recovery when static correlation dominates.

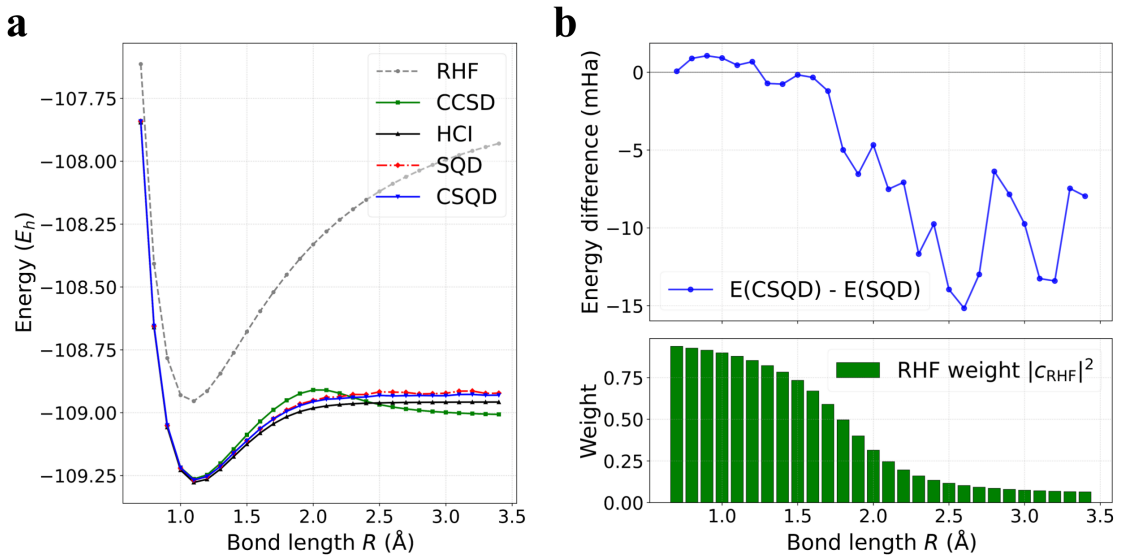


Fig. 2 Dissociation of N_2 : Comparison of CSQD with SQD and classical references. (a) Total energies along the N–N bond-stretching coordinate R for RHF, CCSD, HCI, SQD, and CSQD (BMM, $K = 5$). HCI provides a high-accuracy classical benchmark within the chosen active space (CCSD is non-variational). (b) Upper panel: energy difference $\Delta E(R) = E_{\text{CSQD}}(R) - E_{\text{SQD}}(R)$ in mHa. Negative values indicate a lower variational energy obtained by CSQD. Lower panel: RHF determinant weight $|c_{\text{RHF}}|^2$ (squared coefficient of the RHF determinant in the HCI expansion), which decreases upon bond stretching, reflecting the multireference character. At each R , SQD and CSQD are evaluated from the same quantum inputs and compared at a matched final projected-subspace dimension $\dim(\mathcal{V}) = d_{\text{max}}^2$ with $d_{\text{max}} = 2000$.

We now quantify the robustness of this behavior across clustering models and across $K = 2-5$ at $\dim(\mathcal{V}) = 4 \times 10^6$ ($d_{\text{max}} = 2000$). In the strongly correlated (stretched-bond) regime ($R \geq 1.5R_e$), CSQD yielded lower variational energies ($\Delta E < 0$) in all 72 tested BMM cases and in 71 out of 72 tested k -modes cases. Here, the 72 cases corresponded to 18 stretched-bond geometries evaluated at four distinct values of $K \in \{2, 3, 4, 5\}$. For BMM, the energy difference spanned $\Delta E \in [-15.67, -1.21]$ mHa, with a median and mean of -8.77 and -9.33 mHa, respectively. For k -modes, the energy difference spanned $\Delta E \in [-15.95, +1.19]$ mHa, with a median and mean of -7.68 and -7.45 mHa, respectively. The single instance where SQD yielded a lower energy occurred at $K = 2$ and $R = 2.8$ \AA ($\Delta E = +1.19$ mHa). Overall, this highly consistent advantage in the strongly correlated regime (143 out of 144 tested cases) indicated that the dominant contribution was the cluster-adaptive recovery guided by cluster-resolved references, rather than a particular choice of clustering model or K .

By contrast, in the weakly correlated region ($R < 1.5R_e$), SQD yielded lower variational energies than CSQD in the majority of settings. At $d_{\text{max}} = 2000$ across $K = 2-5$, SQD yielded lower energies in 33/40 BMM cases and 38/40 k -modes cases. The corresponding energy differences spanned $\Delta E \in [-0.77, +3.45]$ mHa for BMM and $\Delta E \in [-0.53, +4.57]$ mHa for k -modes, with medians and means of $+1.16$ and $+1.17$ mHa (BMM) and $+1.72$ and $+1.91$ mHa (k -modes), respectively. This behavior is consistent with a near single-reference regime, where a single global reference occupancy vector already provides an effective guide for particle-number recovery.

At $d_{\text{max}} = 2000$, the cumulative wall-clock time for classical post-processing (sum over the 28 geometries) was 161.8 h for SQD. Across CSQD settings, the corresponding totals ranged from 168.9–175.4 h for BMM ($K = 2-5$) and 166.5–171.6 h for k -modes ($K = 2-5$), implying overheads of 4.4–8.5% and 2.9–6.0%, respectively.

2.4 [2Fe–2S] Cluster: Strong Correlation Benchmark

Iron–sulfur (Fe–S) clusters are stringent benchmarks for strong correlation, with dense, strongly multireference low-energy manifolds. We studied the synthetic $[\text{Fe}_2\text{S}_2(\text{SCH}_3)_4]^{2-}$ complex (abbreviated [2Fe–2S]) [37] using the same localized-orbital active-space Hamiltonian as in Ref. [26]: an

Table 1 [2Fe–2S] **variational energies from SQD and CSQD under identical quantum samples.** Results are reported for $d_{\max} \in \{1000, 1500, 2000\}$ (with final $\dim(\mathcal{V}) = d_{\max}^2$). Energies are in E_h and $\Delta E \equiv E_{\text{CSQD}} - E_{\text{SQD}}$ is in mHa. Negative ΔE indicates an improvement by CSQD. Values are rounded to 5 decimal places in E_h and 2 decimal places in mHa.

Method	$\dim(\mathcal{V}) = 1.00 \times 10^6$		$\dim(\mathcal{V}) = 2.25 \times 10^6$		$\dim(\mathcal{V}) = 4.00 \times 10^6$	
	$E (E_h)$	ΔE (mHa)	$E (E_h)$	ΔE (mHa)	$E (E_h)$	ΔE (mHa)
SQD	-116.39387	0.00	-116.41088	0.00	-116.43666	0.00
BMM ($K=2$)	-116.41751	-23.65	-116.42550	-14.62	-116.46693	-30.27
BMM ($K=3$)	-116.41804	-24.17	-116.42712	-16.24	-116.47723	-40.57
BMM ($K=4$)	-116.41728	-23.41	-116.42632	-15.44	-116.47366	-37.00
BMM ($K=5$)	-116.41599	-22.13	-116.44445	-33.58	-116.48219	-45.53
k -modes ($K=2$)	-116.41531	-21.44	-116.43242	-21.54	-116.46926	-32.60
k -modes ($K=3$)	-116.41494	-21.07	-116.43738	-26.50	-116.47500	-38.34
k -modes ($K=4$)	-116.41545	-21.58	-116.42510	-14.22	-116.47277	-36.11
k -modes ($K=5$)	-116.41451	-20.64	-116.42548	-14.60	-116.47376	-37.10

effective (30e,20o) model spanning Fe(3d) and S(3p) orbitals derived from a BP86 calculation [43, 44] with a TZP-DKH basis [45] and a spin-free X2C treatment [46, 47].

Crucially, we did not perform any new quantum sampling for this benchmark. Instead, we reused the measurement dataset [48] released with Ref. [26] as input to both SQD and CSQD. The dataset consists of $\sim 2.46 \times 10^6$ computational-basis measurement outcomes generated using the SQD sampling protocol. Details of dataset generation and mitigation are provided in Methods.

To enable a controlled comparison, we swept the target projected-subspace size $\dim(\mathcal{V}) = d_{\max}^2$ with $d_{\max} \in \{1000, 1500, 2000\}$. For CSQD, we swept the clustering model (BMM or k -modes) and the number of clusters $K \in \{2, 3, 4, 5\}$. In the [2Fe–2S] benchmark, the released sample set was sufficiently large that both SQD and CSQD achieved the target dimension $\dim(\mathcal{V}) = d_{\max}^2$ in the first iteration, so we ran the self-consistent loop for at most 10 iterations for both methods. We constructed $B = 10$ independent batches per iteration and reported the minimum energy attained across all iterations and batches. To enforce a matched variational budget during iterations, in each batch we drew sufficient strings such that, after merging newly sampled and carry-over strings and removing duplicates, the unique single-spin pool in each spin sector typically reached d_{\max} strings. All classical post-processing was performed as single-node jobs on identical CPU resources (64 cores on a 256-core AMD EPYC 9755 node with 1 TB RAM).

Table 1 summarizes the final variational energies for SQD and CSQD across all tested settings at each final projected-subspace dimension $\dim(\mathcal{V})$ (equal to d_{\max}^2). Across all $d_{\max} \in \{1000, 1500, 2000\}$ and clustering choices (BMM/ k -modes with $K = 2$ –5), CSQD yielded lower variational energies than SQD in every tested case (24/24). The corresponding energy reductions ranged from 20.64 to 24.17 mHa at $\dim(\mathcal{V}) = 1.00 \times 10^6$, from 14.22 to 33.58 mHa at $\dim(\mathcal{V}) = 2.25 \times 10^6$, and from 30.27 to 45.53 mHa at $\dim(\mathcal{V}) = 4.00 \times 10^6$.

The classical post-processing cost of CSQD remained comparable to that of SQD under identical compute resources, with additional work primarily arising from clustering and cluster-wise recovery updates. For $\dim(\mathcal{V}) = 1.00 \times 10^6$, SQD required 5.85 h, while CSQD ranged from 5.57 to 8.16 h. For $\dim(\mathcal{V}) = 2.25 \times 10^6$, SQD required 16.56 h, while CSQD ranged from 15.11 to 23.44 h. For $\dim(\mathcal{V}) = 4.00 \times 10^6$, SQD required 27.25 h, while CSQD ranged from 32.96 to 36.10 h. Overall, CSQD was at most 1.42 \times slower than SQD across all tested settings, and detailed timings are provided in the Supplementary Information.

To gain insight into the energy improvements of CSQD on [2Fe–2S], Fig. 3 examines a representative setting that attained the largest lowering in Table 1 (BMM, $K = 5$, $d_{\max} = 2000$). Fig. 3a reports the iteration-wise energy history, where the plotted value at each iteration is the lowest energy observed up to and including that iteration across all batches. Although both SQD and CSQD already reached the target projected dimension $\dim(\mathcal{V}) = d_{\max}^2$ in the first iteration for this dataset, the energies continued to improve due to the self-consistent recovery updates, which

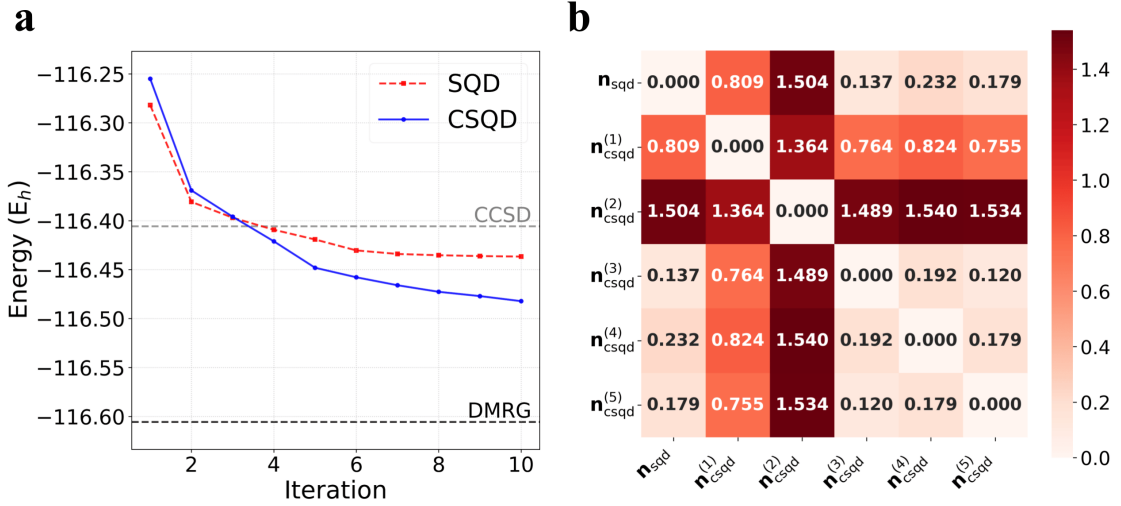


Fig. 3 [2Fe–2S] iteration-wise energy trajectories and reference vector separation in CSQD. **(a)** Iteration-wise lowest variational energies for SQD and CSQD (BMM, $K = 5$) at $d_{\text{max}} = 2000$. At each iteration, both methods were evaluated at the fixed projected-subspace dimension $\dim(\mathcal{V}) = d_{\text{max}}^2 = 4 \times 10^6$, and the plotted value is the lowest energy observed so far across all batches and iterations. Horizontal dashed lines indicate the CCSD and DMRG energies for the same effective active-space Hamiltonian, providing single-reference and high-accuracy classical baselines, respectively. **(b)** Heatmap of one-half the Manhattan distance (L_1) computed for all pairs among the SQD global reference occupation vector \mathbf{n}_{SQD} and the CSQD cluster-specific reference occupation vectors $\mathbf{n}_{\text{CSQD}}^{(k)}$. The values can be interpreted as the effective number of occupation swaps—that is, the total occupation weight, in electrons, required to transform one reference pattern into another. Larger values indicate more strongly separated occupation patterns.

retained carry-over candidates and augmented them with newly sampled configurations under a fixed variational budget. Within the 10 self-consistent iterations performed here, SQD exhibited diminishing energy improvements and appeared to approach a plateau, whereas CSQD continued to decrease through the final iteration and ultimately attained a lower variational energy, consistent with Table 1. For example, SQD improved by ~ 0.87 mHa (iteration 8 \rightarrow 9) and ~ 0.52 mHa (9 \rightarrow 10), whereas CSQD dropped by ~ 4.39 mHa (8 \rightarrow 9) and ~ 5.16 mHa (9 \rightarrow 10). The CCSD and density matrix renormalization group (DMRG) [49] reference energies were taken from the benchmark data [48] released with Ref. [26].

To interpret Fig. 3b, we note that each reference occupation vector \mathbf{n} is normalized to satisfy the electron-number constraint in a given spin sector, $\sum_p n_p = N_\sigma$, and represents the cluster-averaged occupations of the orbitals. In this sense, \mathbf{n} can be interpreted as a centroid in occupation space that summarizes the configurations assigned to that cluster. We quantify the separation between two such occupations using one half of the Manhattan (L_1) distance,

$$\eta_{ij} \equiv \frac{1}{2} \left\| \mathbf{n}^{(i)} - \mathbf{n}^{(j)} \right\|_1 = \frac{1}{2} \sum_p \left| n_p^{(i)} - n_p^{(j)} \right|. \quad (3)$$

Because \mathbf{n} is expressed in electron units, η_{ij} is also measured in electrons and captures the total occupation weight that must be redistributed among orbitals to transform one set of orbital occupations into another. Throughout, we compare single-spin occupation vectors. For SQD, we use the α/β -averaged occupations, $\mathbf{n}_{\text{SQD}} \equiv (\mathbf{n}_{\text{SQD},\alpha} + \mathbf{n}_{\text{SQD},\beta})/2$, which is appropriate in the $S_z = 0$ sector where $\mathbf{n}_{\text{SQD},\alpha} = \mathbf{n}_{\text{SQD},\beta}$ in the ideal spin-inversion-symmetric limit.

Fig. 3b visualizes the matrix of pairwise distances η_{ij} computed between reference occupation vectors, including the SQD global reference and the CSQD cluster-resolved references (BMM, $K = 5$). The distances separate the references into three groups. Clusters 3–5 form a tight group: they lie close to the SQD reference ($\eta \approx 0.12$ – 0.23) and also have small mutual separations (typically $\eta < 0.24$). By contrast, Cluster 1 is at an intermediate distance from both SQD ($\eta \approx 0.81$) and

Clusters 3–5 ($\eta \approx 0.75$ – 0.82). Finally, Cluster 2 is the most distinct reference, with large separations from SQD ($\eta \approx 1.50$) and from all other CSQD clusters ($\eta \approx 1.36$ – 1.54).

Motivated by Fig. 3b, we focus on Clusters 1 and 2, which are the most separated from the SQD global reference occupation vector in this setting ($\eta \approx 0.81$ and $\eta \approx 1.50$, respectively). To assess the role of cluster-specific configurations, we excluded the single-spin strings unique to each cluster from the pooled candidate set and recomputed the final variational energy via projection and diagonalization. Out of the 2,000 single-spin strings comprising the final variational subspace, Cluster 1 contributed 294 strings, of which 100 were found to be exclusive to this cluster. Similarly, Cluster 2 accounted for 235 strings, with 104 of these being unique configurations not identified by any other cluster. Removing the 100 strings unique to Cluster 1 reduced the projected dimension to $(2000 - 100)^2 = 3.61 \times 10^6$ and raised the energy from $-116.48219 E_h$ to $-116.47449 E_h$, corresponding to $+7.70$ mHa, whereas removing the 104 strings unique to Cluster 2 reduced the projected dimension to $(2000 - 104)^2 \sim 3.59 \times 10^6$ and raised the energy to $-116.48160 E_h$, corresponding to $+0.59$ mHa.

Notably, despite its large separation from the SQD reference ($\eta \approx 1.50$), Cluster 2 contributed little through its cluster-exclusive configurations ($+0.59$ mHa upon removal), suggesting it may be an artifact of residual sampling noise or recovery procedures. We therefore refrain from assigning a definitive physical interpretation to Cluster 2 in this benchmark. By comparison, Cluster 1 showed a substantially larger marginal contribution ($+7.70$ mHa), supporting the view that CSQD identified at least one energetically meaningful alternative occupancy pattern beyond the global-reference description in this experiment.

3 Discussion

Summary of results

Strongly correlated systems often exhibit intrinsically multimodal distributions over electronic configurations, reflecting the multiconfigurational character of the underlying wave function. In SQD [26], particle-number symmetry is restored from noisy samples using a single global reference occupancy vector, which is updated in a self-consistent loop. In a multimodal setting, this reference may converge to a mixed average over multiple modes, smearing mode-specific structure and potentially underrepresenting low-weight but physically important modes. To address this potential limitation, we introduced CSQD, which clusters quantum samples via unsupervised learning and performs particle-number recovery using cluster-specific, self-consistently updated reference occupancy vectors. This mode-aware recovery better aligns symmetry restoration with the intrinsic multimodality of strongly correlated wave functions while incurring only modest additional classical post-processing overhead.

We benchmarked CSQD against SQD on two representative problems: the dissociation of N_2 in a (10e,26o) active space and the strongly multireference [2Fe–2S] cluster in an effective (30e,20o) active space. In each benchmark, we used identical quantum samples as input for SQD and CSQD and evaluated both methods at matched final projected-subspace dimensions $\dim(\mathcal{V})$. For N_2 at $\dim(\mathcal{V}) = 4 \times 10^6$, the SQD–CSQD comparison exhibited a clear crossover: SQD was often slightly lower near equilibrium, whereas CSQD was consistently lower in the stretched-bond (strongly correlated) regime ($R \geq 1.5R_e$). Defining $\Delta E \equiv E_{\text{CSQD}} - E_{\text{SQD}}$, we observed $\Delta E < 0$ in 143 out of 144 tested settings in the stretched-bond regime, with the largest reductions reaching ~ 15.95 mHa, while any SQD advantage near equilibrium remained below ~ 4.57 mHa. For [2Fe–2S], we performed no new quantum sampling, instead reusing the fixed measurement dataset [48] released with Ref. [26]. Across clustering choices (BMM/ k -modes with $K = 2$ – 5) and $\dim(\mathcal{V}) \in \{1.00, 2.25, 4.00\} \times 10^6$, CSQD yielded lower variational energies in every tested case (24/24), with energy lowerings on the order of tens of millihartree up to 45.53 mHa at $\dim(\mathcal{V}) = 4.00 \times 10^6$. Overall, CSQD incurred a limited additional classical post-processing cost, being at most $1.42\times$ slower than SQD across all tested settings.

To probe mode separation in [2Fe–2S], we compared the SQD global reference occupancy vector with CSQD’s cluster-specific reference occupancy vectors and analyzed their pairwise separations. In the representative setting of Fig. 3b (BMM, $K = 5$, $\dim(\mathcal{V}) = 4 \times 10^6$), the separation metric η defined in Eq. (3) indicated that, alongside clusters whose occupation centroids remained

close to the SQD global reference, two clusters exhibited substantially separated occupation centroids. Motivated by this separation, we assessed the marginal contribution of cluster-exclusive configurations by performing projection and diagonalization with an exclusion test. Removing the strings assigned exclusively to one of the separated clusters increased the variational energy by ~ 7.70 mHa, whereas the analogous removal for the other separated cluster changed the energy by ~ 0.59 mHa, so we refrain from over-interpreting the latter. Overall, these observations suggest that, in this benchmark, CSQD captured at least one energetically meaningful alternative configurational mode beyond a single global-reference description. This is consistent with the premise that multimodality can limit global-reference recovery and that cluster-resolved recovery can mitigate this limitation.

Composability with SQD-based extensions

Existing SQD-based extensions can be broadly grouped into two categories. First, some approaches use SQD-derived samples and/or wave functions as inputs to high-accuracy classical methods, including excited-state extensions [28], ph-AFQMC [30], and quantum embedding [31], to improve accuracy and broaden applicability. Second, other variants aim to improve the efficiency of SQD itself under limited-shot and noisy conditions by enhancing the sampling process, for example via Krylov subspace-based sampling [29], or by expanding the effective configuration set via generative modeling [32]. In contrast, CSQD targets a different bottleneck: given a fixed set of noisy samples, it strengthens the recovery step by making it mode-aware. This is particularly relevant in strongly correlated, multimodal regimes, where a single global reference can become over-averaged and smear mode-specific structure.

From this perspective, CSQD is naturally compatible with the SQD variants discussed above and can be viewed as a modular enhancement to the recovery stage. For example, in excited-state extensions such as Ext-SQD [28], which enlarge the configuration space starting from SQD-derived configurations, CSQD can provide a mode-resolved recovered configuration set that may improve subsequent subspace expansion. Likewise, for approaches that use SQD outputs as seeds for higher-accuracy classical solvers, such as ph-AFQMC [30] and quantum embedding frameworks [31], CSQD has the potential to improve the quality of the seed or trial wave function and thereby reduce bias or improve efficiency. Finally, because CSQD targets mode averaging in recovery rather than the sampling stage, it is complementary to improved sampling and/or generation-oriented variants such as SKQD [29] and PIGen-SQD [32], motivating future work on integrated workflows. While systematic benchmarking of such combined workflows is beyond the scope of this work, we present CSQD as a complementary refinement of the recovery stage within the broader SQD workflow, and leave detailed integration and optimization to future work.

Implementation considerations for CSQD

A key implementation choice in CSQD is to operate on single-spin occupation strings rather than clustering full (α, β) bitstrings. In the $S_z = 0$ singlet-target setting, the configurations (μ_α, μ_β) and (μ_β, μ_α) are physically equivalent under spin inversion, yet clustering in the full $2N_{\text{MO}}$ bitstring space can separate such pairs when μ_α and μ_β are far apart in Hamming distance. Pooling and clustering single-spin strings treat the two spin sectors on equal footing, naturally preserving this physical equivalence.

Moreover, this single-spin approach can increase statistical efficiency by effectively expanding the sample count, yielding up to $2N_{\text{meas}}$ single-spin strings from N_{meas} measurements. When the projected subspace is subsequently formed on the product space of up to $2N_{\text{meas}}$ pooled single-spin strings, the resulting set of candidate full configurations can scale quadratically, yielding $\mathcal{O}(N_{\text{meas}}^2)$ possible α - β pairings before any truncation or deduplication. This implicit quadratic expansion may mitigate sensitivity to the sampling redundancy discussed in Ref. [50], where enlarging the discovered configuration pool can require an increasingly large number of additional measurements as new samples increasingly yield redundant configurations. We do not attempt to quantify this potential mitigation here, and in practice it may trade measurement efficiency for higher classical clustering and/or recovery overhead.

Although clustering is performed in the single-spin space, CSQD assigns an importance weight to each single-spin string using the variational solution on the product space $\mathcal{D} \times \mathcal{D}$. Concretely, the

importance weight assigned to a single-spin string aggregates the squared configuration interaction (CI) amplitudes of all determinants in which that string appears, meaning that an important determinant (μ_α, μ_β) contributes simultaneously to the importance weights of μ_α and μ_β (see Methods). Consequently, determinants with large-magnitude CI amplitudes tend to induce large importance weights for both of their spin components, increasing the likelihood that μ_α and μ_β are simultaneously retained in \mathcal{D} . Whenever both components are retained, the corresponding (μ_α, μ_β) determinant is explicitly present in the variational space $\mathcal{D} \times \mathcal{D}$ and can contribute to the projected diagonalization. This construction does not enforce the empirical pairing structure during clustering. Rather, the joint α - β correlations are reintroduced and can be captured to the extent permitted by $\mathcal{D} \times \mathcal{D}$ at the projected diagonalization stage.

In this work we focus on $S_z = 0$ singlet ground states, consistent with the benchmark problems considered. However, the CSQD principle—cluster-specific reference occupancies and cluster-specific recovery—does not rely on the singlet restriction. Extensions to other sectors defined by N_α and N_β can be implemented by maintaining spin-sector-specific string pools and reference vectors, while spin targeting such as singlet or triplet selection can be handled at the projected diagonalization stage using standard constraints or penalties.

Finally, our results indicate that CSQD provides consistent benefits over SQD in strongly correlated regimes across the clustering choices tested. At the same time, the attained accuracy can depend on the clustering model and its hyperparameters, suggesting an open direction for further refinement of the clustering stage. In our benchmarks, BMM often yields slightly better accuracy than k -modes, although this advantage is not uniform across systems and regimes. We also do not observe a consistent dependence on the number of clusters K (detailed parameter sweeps are reported in the Supplementary Information). These observations motivate future work for improving robustness and practical performance. Further improvements may be gained by moving beyond hard assignments. In the present implementation, we partially relax hard boundaries by accumulating cluster membership information across iterations (see Methods). A principled approach based on fully soft membership assignments could provide additional robustness by naturally propagating uncertainty in cluster boundaries into the reference updates. Physically informed clustering criteria, as well as hybrid approaches that incorporate a coarse classical pre-refinement prior to clustering, may also further improve stability. Developing more systematic soft-membership updates and adaptive choices for the clustering model and K represents a natural direction for future work.

4 Methods

4.1 Hamiltonian, Mapping, and Determinant Representation

Our goal is to estimate the ground-state energy and wave function of the electronic Born–Oppenheimer Hamiltonian written in second quantization over a finite orthonormal molecular-orbital basis, as defined in Eq. (1). We denote by $\hat{a}_{p\sigma}^\dagger$ and $\hat{a}_{p\sigma}$ the fermionic creation and annihilation operators acting on spin orbital (p, σ) , and define the number operator $\hat{n}_{p\sigma} = \hat{a}_{p\sigma}^\dagger \hat{a}_{p\sigma}$. Unless otherwise stated, we use atomic units for electronic-structure quantities: lengths are measured in bohr and energies in hartree. Geometric parameters (e.g., bond lengths) are reported in angstroms (Å) by convention. For nonrelativistic all-electron calculations, the nuclear repulsion energy E_{nuc} , the one-electron integrals h_{pr} , and the two-electron integrals $(pr|qs)$ are defined as

$$E_{\text{nuc}} = \sum_{a < b}^{N_{\text{nuc}}} \frac{Z_a Z_b}{\|\mathbf{R}_a - \mathbf{R}_b\|}, \quad (4)$$

$$h_{pr} = \int d\mathbf{r} \phi_p^*(\mathbf{r}) \left[-\frac{1}{2} \nabla^2 - \sum_{a=1}^{N_{\text{nuc}}} \frac{Z_a}{\|\mathbf{r} - \mathbf{R}_a\|} \right] \phi_r(\mathbf{r}), \quad (5)$$

$$(pr|qs) = \int d\mathbf{r}_1 \int d\mathbf{r}_2 \frac{\phi_p^*(\mathbf{r}_1) \phi_r(\mathbf{r}_1) \phi_q^*(\mathbf{r}_2) \phi_s(\mathbf{r}_2)}{\|\mathbf{r}_1 - \mathbf{r}_2\|}, \quad (6)$$

where N_{nuc} , \mathbf{R}_a , and Z_a denote the number of nuclei, their positions, and atomic numbers, respectively. In scalar-relativistic (spin-free) and/or active-space calculations, the indices p, r, q, s

label active-space orbitals, and the quantities E_{nuc} , h_{pr} , and $(pr|qs)$ are modified to account for scalar-relativistic effects and/or the effective potential generated by inactive electrons.

We represent many-electron basis states using Slater determinants and map them to qubit computational-basis states via the Jordan–Wigner transformation. In this mapping, each qubit encodes the occupancy of a spin orbital, and computational-basis measurements return bitstrings $x \in \{0, 1\}^{2N_{\text{MO}}}$, where N_{MO} is the number of spatial orbitals. Each bitstring x corresponds uniquely to a determinant $|x\rangle$ obtained by applying creation operators in a fixed canonical order of spin orbitals according to the occupation pattern (see Eq. (2)). Because the Hamiltonian in Eq. (1) is spin-conserving in the absence of spin–orbit coupling, the numbers of α and β electrons are conserved. The number of spin- σ electrons in configuration x is $N_\sigma(x) = \sum_p x_{p\sigma}$, and x lies in the correct particle sector if it satisfies

$$(N_\alpha(x), N_\beta(x)) = (N_\alpha, N_\beta), \quad (7)$$

i.e., the spin-resolved electron counts computed from the bitstring match the target sector of the molecular problem. In the benchmarks studied in this work, we estimate the ground-state energy in the $S_z = 0$ sector (i.e., $N_\alpha = N_\beta \equiv N_\sigma$).

4.2 CSQD: Clustering-Based Configuration Recovery

CSQD takes computational-basis samples and constructs compact determinant subspaces for classical projection and diagonalization. Algorithm 1 provides a high-level schematic of the CSQD loop, including clustering of single-spin strings, cluster-adaptive particle-number symmetry recovery (pool refinement), and iterative subspace construction with carry-over. We next describe CSQD in detail, including clustering, subsampling, reference-vector updates, and projection–diagonalization steps.

Input samples and clustering

From quantum measurements, we obtain N_{meas} computational-basis outcomes, collected in a set $\mathcal{X} \subset \{0, 1\}^{2N_{\text{MO}}}$. For an observed outcome $x \in \mathcal{X}$, x is a full bitstring encoding spin-orbital occupations and $\text{Pr}(x)$ denotes its empirical probability (normalized frequency) over \mathcal{X} . We split each x into two single-spin strings,

$$x = (\mu_\alpha, \mu_\beta), \quad \mu_\sigma \in \{0, 1\}^{N_{\text{MO}}} \quad (\sigma \in \{\alpha, \beta\}), \quad (8)$$

and use the single-spin strings μ as the fundamental objects in CSQD. We pool the single-spin strings observed across all measurement outcomes, deduplicate them, and form a pooled set \mathcal{X}_μ . For each $\mu \in \mathcal{X}_\mu$, we assign a pooled empirical weight $\pi(\mu)$ defined by

$$\pi(\mu) = \frac{1}{2} \sum_{x \in \mathcal{X}} \text{Pr}(x) [\mathbf{1}(\mu_\alpha(x) = \mu) + \mathbf{1}(\mu_\beta(x) = \mu)], \quad \sum_{\mu \in \mathcal{X}_\mu} \pi(\mu) = 1, \quad (9)$$

where $(\mu_\alpha(x), \mu_\beta(x))$ is the decomposition of x in Eq. (8), and $\mathbf{1}(\cdot)$ equals 1 if the argument is true and 0 otherwise.

We partition the pooled set \mathcal{X}_μ into K clusters $\{\mathcal{C}_k\}_{k=1}^K$, and define the within-cluster normalized weight $\pi_k(\mu) = \pi(\mu)/w_k$ for $\mu \in \mathcal{C}_k$, where w_k is given in Eq. (10). In this work, we employ k -modes [39, 40] and BMM [41, 42] for clustering. We perform clustering once per geometry and keep cluster assignments fixed throughout the CSQD iterations. The cluster sampling weight and the per-batch allocation are

$$w_k = \sum_{\mu \in \mathcal{C}_k} \pi(\mu), \quad m_k = \lceil w_k S \rceil, \quad (10)$$

Algorithm 1 CSQD: Clustering-Based Configuration Recovery (high-level)

Require: Samples $\mathcal{X} \subset \{0,1\}^{2N_{\text{MO}}}$ obtained from N_{meas} measurements with empirical probabilities $\Pr(x)$; target (N_α, N_β) with $N_\alpha = N_\beta \equiv N_\sigma$ ($S_z = 0$). Params: K (clusters), B (batches per iteration), S (per-batch new-sample budget), d_{max} (max single-spin string budget), T (max iterations), τ (carry-over threshold), $(\varepsilon_E, \varepsilon_n)$ (stopping tolerances).

Ensure: Lowest-energy found subspace solution $(E^*, C^*, \mathcal{D}^*)$ and $\{\mathbf{n}^{(k)}\}_{k=1}^K$, where C^* denotes CI coefficients on $\mathcal{D}^* \times \mathcal{D}^*$.

Preprocess. Split $x \in \mathcal{X}$ into single-spin strings μ ; pool unique μ with weights; cluster into $\{\mathcal{C}_k\}_{k=1}^K$ with weights w_k ; set $m_k \leftarrow \lceil w_k S \rceil$.

- 1: Initialize $\mathbf{n}_{\text{raw}}^{(k)}$ as the weighted sum of string occupancies in \mathcal{C}_k .
- 2: Postselect particle-number-correct outcomes x and re-pool their single-spin strings.
- 3: Assign postselected strings to clusters to form $\{\mathcal{C}_k^C\}$; set $\mathcal{C}_k^I = \mathcal{C}_k \setminus \mathcal{C}_k^C$.
- 4: $E^* \leftarrow +\infty$; $\mathcal{D}^* \leftarrow \emptyset$; $C^* \leftarrow \emptyset$.

Setup (t=1). Use only the postselected correct pools.

- 5: $\tilde{\mathcal{C}}_k \leftarrow \mathcal{C}_k^C$ for all k .
- 6: **for** $b = 1, \dots, B$ **do**
- 7: Sample \mathcal{D}_{new} by drawing m_k elements from each $\tilde{\mathcal{C}}_k$; if a cluster has fewer than m_k postselected strings, fill the deficit by sampling synthetic strings guided by $\mathbf{n}_{\text{raw}}^{(k)}$ under the particle-number constraint.
- 8: Construct $\mathcal{D} \leftarrow \mathcal{D}_{\text{new}}$; deduplicate (and, if needed, truncate to d_{max}).
- 9: Solve the projected problem on $\text{span}(\mathcal{D} \times \mathcal{D})$ to obtain (E, C) ; if $E < E^*$, update $(E^*, C^*, \mathcal{D}^*)$.
- 10: **end for**
- 11: $E_{\text{prev}} \leftarrow E^*$; $\mathbf{n}_{\text{prev}}^{(k)} \leftarrow \mathbf{n}_{\text{raw}}^{(k)}$.
- 12: **for** $t = 2, \dots, T$ **do**
- 13: Update $\mathbf{n}^{(k)}$ from (C^*, \mathcal{D}^*) (membership-weighted, coefficient-weighted occupancies with particle-number normalization; see Eq. (16)).
- 14: Refine pools: for each k , map $\mu \in \mathcal{C}_k^I$ to corrected strings via biased bit flips guided by $\mathbf{n}^{(k)}$; set $\tilde{\mathcal{C}}_k \leftarrow \mathcal{C}_k^C \cup \tilde{\mathcal{C}}_k^I$.
- 15: **for** $b = 1, \dots, B$ **do**
- 16: Sample \mathcal{D}_{new} from $\tilde{\mathcal{C}}_k$ and compute $I_{\text{new}}(\mu)$ (see Eq. (19)).
- 17: Select carry-over $\mathcal{D}_{\text{carry}}$ from \mathcal{D}^* by thresholding C^* at τ and compute $I_{\text{carry}}(\mu)$ (see Eq. (21)).
- 18: Merge and deduplicate: $\mathcal{D} \leftarrow \mathcal{D}_{\text{new}} \cup \mathcal{D}_{\text{carry}}$; compute $I(\mu) = I_{\text{new}}(\mu) + I_{\text{carry}}(\mu)$ and retain the top d_{max} strings by $I(\mu)$.
- 19: Solve the projected problem on $\text{span}(\mathcal{D} \times \mathcal{D})$ to obtain (E, C) ; if $E < E^*$, update $(E^*, C^*, \mathcal{D}^*)$.
- 20: **end for**
- 21: **if** $|E^* - E_{\text{prev}}| < \varepsilon_E$ **and** $\max_k \|\mathbf{n}^{(k)} - \mathbf{n}_{\text{prev}}^{(k)}\|_\infty < \varepsilon_n$ **then**
- 22: **break**
- 23: **end if**
- 24: $E_{\text{prev}} \leftarrow E^*$; $\mathbf{n}_{\text{prev}}^{(k)} \leftarrow \mathbf{n}^{(k)}$.
- 25: **end for**
- 26: **return** $(E^*, C^*, \mathcal{D}^*, \{\mathbf{n}^{(k)}\})$.

where S is the per-batch new-sample budget. We also define the initial (unnormalized) reference occupancy vector for each cluster as

$$\mathbf{n}_{\text{raw}}^{(k)} = \sum_{\mu \in \mathcal{C}_k} \pi(\mu) \mu, \quad (11)$$

i.e., the probability-weighted sum of string occupations.

Particle-number postselection

CSQD proceeds in iterations indexed by $t = 1, \dots, T$. At $t = 1$, we restrict to measurement samples whose full bitstring x satisfies the target particle numbers,

$$\text{hw}(\mu_\alpha) = \text{hw}(\mu_\beta) = N_\sigma, \quad (12)$$

where $\text{hw}(\cdot)$ denotes the Hamming weight. We re-pool the single-spin strings from these postselected samples, map them to the precomputed clusters $\{\mathcal{C}_k\}$, and form cluster-wise pools of particle-number-correct strings. For later pool refinement, we also partition each cluster into a correct particle-number subset \mathcal{C}_k^C and an incorrect subset $\mathcal{C}_k^I = \mathcal{C}_k \setminus \mathcal{C}_k^C$.

Iteration $t = 1$: initial subspace construction

For each cluster k , we draw up to m_k particle-number-correct strings without replacement from the postselected pool assigned to \mathcal{C}_k , with probabilities proportional to $\pi_k(\mu)$. If the number of available postselected strings in cluster k is smaller than m_k , we fill the deficit by generating additional particle-number-correct strings guided by $\mathbf{n}_{\text{raw}}^{(k)}$: we sample N_σ occupied orbital indices without replacement using weights proportional to $\mathbf{n}_{\text{raw}}^{(k)}$. We then pool the selected strings across clusters, remove duplicates, and form the initial single-spin string set \mathcal{D} .

Projected diagonalization

Given a selected set of single-spin strings \mathcal{D} , we form the product-basis $\{|\mu\rangle_\alpha |\nu\rangle_\beta\}_{\mu, \nu \in \mathcal{D}}$ and define the corresponding projector

$$\hat{P}_{\mathcal{D}} = \sum_{\mu \in \mathcal{D}} \sum_{\nu \in \mathcal{D}} |\mu\rangle_\alpha |\nu\rangle_\beta \langle \mu|_\alpha \langle \nu|_\beta. \quad (13)$$

We then construct the projected Hamiltonian $\hat{H}_{\mathcal{D}} = \hat{P}_{\mathcal{D}} \hat{H} \hat{P}_{\mathcal{D}}$ and solve for its lowest eigenpair to obtain the projected energy and CI coefficients on $\mathcal{D} \times \mathcal{D}$. In practice, we solve the projected eigenproblem using PySCF [51, 52] with a Davidson-type iterative eigensolver. Following SQD [26], to target the singlet, we encourage $\hat{S}^2 = 0$ using a spin-penalty, i.e.,

$$\hat{H}_{\mathcal{D}} \mapsto \hat{H}_{\mathcal{D}} + \lambda(\hat{S}^2 - s(s+1))^2, \quad s = 0, \quad (14)$$

with $\lambda > 0$ chosen to suppress spin contamination. In all CSQD and SQD experiments conducted in this study, we set the spin-penalty parameter λ to 0.1. For each iteration, we solve B independent batches and update the current best solution $(E^*, C^*, \mathcal{D}^*)$ when a batch yields a projected energy lower than E^* .

Cluster membership accumulation

For each string μ , CSQD maintains a Boolean membership vector $\mathbf{M}_\mu \in \{0, 1\}^K$ indicating which clusters have produced μ . When constructing each batch, the component corresponding to the sampled cluster is set to 1; if the same string is selected from multiple clusters, memberships are accumulated. Carry-over strings inherit their previous memberships, and overlaps between carry-over and newly sampled strings are also merged via OR. Thus, once a string is ever associated with a cluster, its membership for that cluster remains 1, which partially softens hard cluster boundaries.

Self-consistent update of reference vectors

For iterations $t \geq 2$, the cluster-wise reference occupancy vectors $\mathbf{n}^{(k)}$ are updated from the current best CI coefficients C^* on $\mathcal{D}^* \times \mathcal{D}^*$. We define a string weight

$$w_\mu = \sum_{\nu \in \mathcal{D}^*} |C_{\mu\nu}^*|^2 + \sum_{\nu \in \mathcal{D}^*} |C_{\nu\mu}^*|^2, \quad (15)$$

and update $\mathbf{n}^{(k)}$ by a membership-weighted average of occupancies, followed by particle-number normalization:

$$\mathbf{n}^{(k)} = N_\sigma \frac{\sum_{\mu \in \mathcal{D}^*} M_{\mu,k} w_\mu \mu}{\left\| \sum_{\mu \in \mathcal{D}^*} M_{\mu,k} w_\mu \mu \right\|_1}, \quad (16)$$

where $\|\cdot\|_1$ denotes the sum of vector components and $M_{\mu,k}$ denotes the k th component of the membership vector \mathbf{M}_μ . The normalization enforces $\sum_p n_p^{(k)} = N_\sigma$, so $\mathbf{n}^{(k)}$ can be interpreted as a cluster-resolved reference occupancy profile.

Using the updated $\mathbf{n}^{(k)}$, we refine each cluster pool by correcting particle-number-incorrect strings in \mathcal{C}_k^I to produce particle-number-correct candidates, yielding a refined pool $\tilde{\mathcal{C}}_k = \mathcal{C}_k^C \cup \tilde{\mathcal{C}}_k^I$, where $\tilde{\mathcal{C}}_k^I$ denotes the set of corrected strings obtained from \mathcal{C}_k^I by the procedure below. For a string $\mu \in \mathcal{C}_k^I$, we define a flip score for orbital p as

$$d_p = |\mu_p - n_p^{(k)}|. \quad (17)$$

We use the same modified ReLU weighting as in Ref. [26]:

$$\text{ReLU}(d) = \begin{cases} \delta_0 \frac{d}{f}, & d \leq f, \\ \delta_0 + (1 - \delta_0) \frac{d - f}{1 - f}, & d > f, \end{cases} \quad f = \frac{N_\sigma}{N_{\text{MO}}}. \quad (18)$$

In all experiments, we set $\delta_0 = 0.01$. Let $\Delta_{hw} = \text{hw}(\mu) - N_\sigma$. If $\Delta_{hw} > 0$, we select Δ_{hw} occupied positions to flip $1 \rightarrow 0$; if $\Delta_{hw} < 0$, we select $|\Delta_{hw}|$ unoccupied positions to flip $0 \rightarrow 1$. In both cases, positions are sampled without replacement with probabilities proportional to $\text{ReLU}(d_p)$, and the resulting corrected strings are pooled into $\tilde{\mathcal{C}}_k^I$.

Subsampling, carry-over, and subspace truncation for $t \geq 2$

At each batch, we draw m_k strings from each refined pool $\tilde{\mathcal{C}}_k$ without replacement to form a new candidate set \mathcal{D}_{new} . We assign each $\mu \in \mathcal{D}_{\text{new}}$ a subsampling-derived weight $I_{\text{new}}(\mu)$ as follows: cluster-normalize sampling probabilities, scale by the cluster allocation $m_k / \sum_{\ell=1}^K m_\ell$, and sum weights upon deduplication. Equivalently,

$$I_{\text{new}}(\mu) = \sum_{k: \mu \in \mathcal{D}_{\text{new}}^{(k)}} \hat{\pi}_k(\mu) \frac{m_k}{\sum_{\ell=1}^K m_\ell}, \quad (19)$$

where $\hat{\pi}_k(\mu)$ denotes the sampling probability used within the refined pool $\tilde{\mathcal{C}}_k$, normalized so that $\sum_{\mu \in \tilde{\mathcal{C}}_k} \hat{\pi}_k(\mu) = 1$, after aggregating and renormalizing weights following correction and deduplication.

To stabilize the subspace across iterations, we also carry over strings from the current best subspace \mathcal{D}^* using a threshold τ on the CI coefficients:

$$\mathcal{D}_{\text{carry}} = \left\{ \mu \in \mathcal{D}^* : \max_{\nu \in \mathcal{D}^*} |C_{\mu\nu}^*| > \tau \text{ or } \max_{\nu \in \mathcal{D}^*} |C_{\nu\mu}^*| > \tau \right\}. \quad (20)$$

Each carry-over string is assigned the carry-over importance

$$I_{\text{carry}}(\mu) = \sum_{\nu \in \mathcal{D}^*} |C_{\mu\nu}^*|^2, \quad \mu \in \mathcal{D}_{\text{carry}}. \quad (21)$$

In the $S_z = 0$ sector of a spin-free Hamiltonian with identical α/β string pools, the α - and β -marginal weights are equivalent up to an overall factor in the ideal spin-inversion-symmetric limit. Hence, we use the α -marginal $I_{\text{carry}}(\mu) = \sum_{\nu \in \mathcal{D}^*} |C_{\mu\nu}^*|^2$ without loss of generality. We then merge \mathcal{D}_{new} and $\mathcal{D}_{\text{carry}}$, deduplicate identical strings, and define the final importance

$$I(\mu) = I_{\text{carry}}(\mu) + I_{\text{new}}(\mu). \quad (22)$$

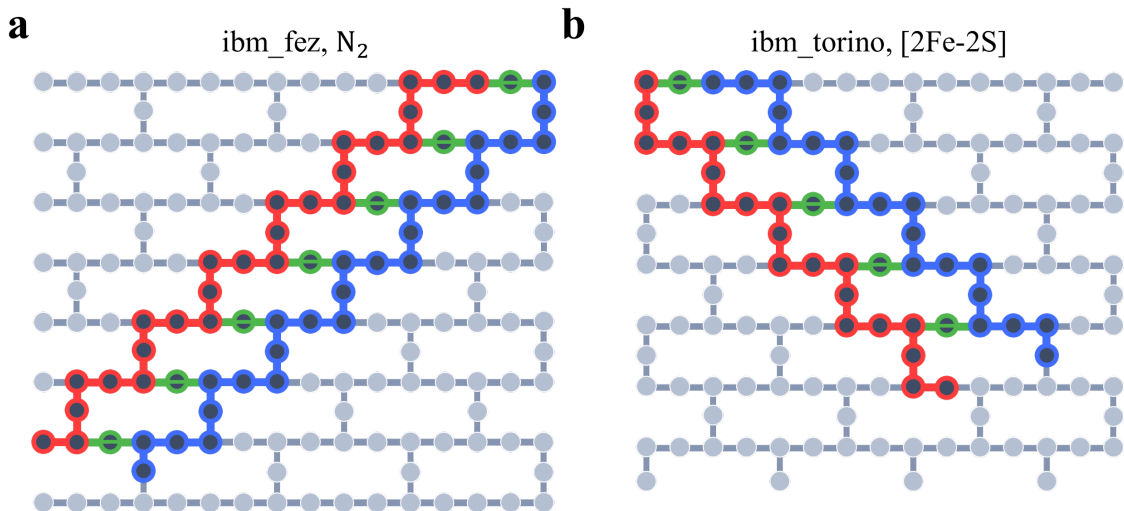


Fig. 4 Hardware mapping on IBM quantum processors. Device schematics showing the qubit layouts and role assignments used in this work: **(a)** N_2 experiment on `ibm_fez` and **(b)** $[2Fe-2S]$ cluster experiment on `ibm_torino`. Qubits are colored by role: α spin-orbitals (red), β spin-orbitals (blue), and auxiliary qubits (green).

Finally, we retain the top d_{\max} strings by $I(\mu)$ to form the working set \mathcal{D} for the projected diagonalization step. As in the $t = 1$ case, this rank-based truncation preferentially retains carry-over strings without imposing a hard constraint. Since the physical weights $I_{\text{carry}}(\mu)$ derived from the wave function coefficients are typically orders of magnitude larger than the statistical sampling weights $I_{\text{new}}(\mu)$, this scheme promotes the prioritization of chemically significant strings during truncation.

Stopping criterion

We terminate the iterations when (i) the improvement in the best energy is below ε_E and (ii) the maximum change in the reference vectors satisfies

$$\max_{k,p} |n_p^{(k)} - n_{\text{prev},p}^{(k)}| < \varepsilon_n. \quad (23)$$

The hyperparameters $(K, B, S, d_{\max}, T, \tau, \varepsilon_E, \varepsilon_n)$ and system-specific settings are reported in the corresponding experimental subsections.

4.3 N_2 Dissociation—Computational Details

Molecular Hamiltonian and active-space definition.

We studied the dissociation curve of N_2 by scanning the internuclear separation R from 0.7 to 3.4 Å in steps of 0.1 Å (28 geometries). All electronic-structure quantities were computed in the cc-pVDZ basis using RHF as the reference. We froze the two lowest-energy core spatial orbitals, yielding an active space of 26 spatial orbitals and 10 active electrons with $(N_\alpha, N_\beta) = (5, 5)$. For each geometry, we constructed the active-space one- and two-electron integrals from the RHF reference using the frozen-core CASCI Hamiltonian construction. We also computed the associated constant energy shift (nuclear repulsion plus frozen-core contribution) and used it throughout the SQD/CSQD post-processing. Unless otherwise stated, all N_2 energies reported in this section include this constant shift.

Quantum circuit construction and sampling.

We followed the circuit-design protocol of Ref. [26] to generate measurement samples for N_2 . We used the LUCJ ansatz [53], a derivative of the UCJ ansatz [54]. Its general form is given by

$$|\Psi\rangle = \prod_{l=1}^L e^{\hat{K}_l} e^{i\hat{J}_l} e^{-\hat{K}_l} |x_{\text{RHF}}\rangle. \quad (24)$$

In this expression, $\hat{K}_l = \sum_{p,r,\sigma} K_{pr}^{(l)} \hat{a}_{p\sigma}^\dagger \hat{a}_{r\sigma}$ is a one-body generator, and $\hat{J}_l = \sum_{p,r,\sigma,\tau} J_{p\sigma,r\tau}^{(l)} \hat{n}_{p\sigma} \hat{n}_{r\tau}$ is a number-diagonal Jastrow operator. We set $L = 1$ to limit circuit depth while retaining flexibility via an additional final orbital rotation appended at the end. The sampled state was thus

$$|\Psi\rangle = e^{-\hat{K}_2} e^{\hat{K}_1} e^{i\hat{J}_1} e^{-\hat{K}_1} |x_{\text{RHF}}\rangle, \quad (25)$$

where \hat{K}_1 and \hat{J}_1 correspond to the single ($L = 1$) UCJ layer in Eq. (24), and \hat{K}_2 is an additional one-body rotation applied after the correlated layer. The circuit parameters were obtained from a restricted closed-shell CCSD calculation without additional parameter optimization.

To impose the connectivity-based locality restriction used in the LUCJ construction, we restricted the Jastrow interaction pairs as follows: (i) for same-spin terms, we retained only nearest-neighbor pairs $(p, p+1)$ for $p = 0, \dots, 24$, and (ii) for opposite-spin terms, we retained on-site pairs (p, p) for $p \in \{0, 4, 8, 12, 16, 20, 24\}$, for which the corresponding α and β qubits are separated by a single intermediate qubit (graph distance two) on the heavy-hex topology of IBM devices in Fig. 4a. We constructed the LUCJ circuit using the `ffsim` library [55].

Quantum sampling was performed on the IBM Heron r2 backend `ibm_fez`. The 26-orbital active space was encoded using 52 qubits (two spin sectors). To accommodate a fixed qubit layout on the heavy-hex topology while reducing routing overhead, the sampling circuits occupied 59 device qubits in total, consisting of the 52 spin-orbital qubits and 7 additional routing/auxiliary qubits. The layout and the assignment of α and β spin-orbitals to device qubits are shown in Fig. 4a. With this fixed layout, transpilation to the backend native gate set yielded a sampling circuit containing 1,876 two-qubit gates.

Error mitigation and reset-mitigation postselection.

Each geometry was sampled with a total of 3×10^5 shots. We applied dynamical decoupling [56] using the XpXm sequence and measurement twirling [57] with 32 randomizations and 9375 shots per randomization. To mitigate errors arising from imperfect qubit reset, we employed the reset-mitigation scheme demonstrated in Ref. [26]. This protocol inserts a measurement instruction on all qubits immediately prior to state preparation and discards shots for which the initially measured bitstring differs from the state $0 \cdots 0$. The corresponding final measurement outcomes were then used to form the empirical sample distribution for SQD and CSQD. After reset-mitigation filtering, we retained on average $\sim 1.08 \times 10^5$ measurement outcomes per geometry.

SQD and CSQD settings.

For the SQD baseline, we followed Ref. [26] and utilized the `qiskit-addon-sqd` package [58]. We set the number of batches per iteration to $B = 10$. From the second recovery iteration onward, $S_{\text{full}} = d_{\text{max}}$ full spin-orbital bitstrings (i.e., 52-bit $\alpha\beta$ measurement outcomes) were drawn for each batch from the corrected full-string pool. These samples were augmented with carry-over configurations at the level of full spin-orbital bitstrings. The resulting pool was then split into α and β strings and truncated to at most d_{max} single-spin strings per spin sector prior to the projected diagonalization. The maximum number of configuration-recovery iterations was set to $T_{\text{SQD}} = 11$. We imposed spin-exchange symmetry by symmetrizing the single-spin-string pools (i.e., $\mathcal{D}_\alpha = \mathcal{D}_\beta$).

For CSQD, we used the same target particle number and batching ($B = 10$), with a per-batch new-sample budget of $S_{\text{spin}} = d_{\text{max}}$ single-spin strings and a maximum of $T_{\text{CSQD}} = 10$ iterations. To keep the effective variational dimension budget comparable between SQD and CSQD throughout the recovery iterations, we set $S_{\text{full}} = S_{\text{spin}} = d_{\text{max}}$ so that, after splitting and truncation, each spin-sector pool typically remained close or equal to d_{max} . We swept the number of clusters

$K \in \{2, 3, 4, 5\}$ and considered two clustering methods: weighted k -modes clustering (Huang initialization) [39, 40] and weighted BMM [41]. For both methods, the best fit was selected from 100 random initializations.

For both SQD and CSQD, we truncated the diagonalization subspace by limiting each spin sector to at most d_{\max} single-spin strings. We considered $d_{\max} \in \{1000, 1500, 2000\}$, corresponding to a maximum projected dimension of d_{\max}^2 . We reported results for $d_{\max} = 2000$ in the main text, while other values are provided in the Supplementary Information. Carry-over between iterations used a coefficient threshold of $\tau = 10^{-4}$. Convergence was assessed using $(\varepsilon_E, \varepsilon_n) = (10^{-8}, 10^{-5})$, where ε_E denotes the threshold for energy improvement and ε_n denotes the maximum change in orbital occupancies (infinity norm). Configuration recovery utilized the modified-ReLU flip weighting with $\delta_0 = 0.01$ (see Eq. (18)). Projected diagonalizations targeted the singlet sector (see Eq. (14)). All classical post-processing tasks were executed as single-node jobs on compute nodes with identical hardware specifications (56-core Intel Xeon Gold 6348R with 1 TB RAM).

4.4 [2Fe–2S] Cluster—Computational Details

Molecular Hamiltonian and active-space definition.

We considered the synthetic $[\text{Fe}_2\text{S}_2(\text{SCH}_3)_4]^{2-}$ complex (abbreviated [2Fe–2S]) [37]. Following Ref. [26], we employed the same localized-orbital active-space Hamiltonian with an effective (30e,20o) active space. The active orbitals span the Fe(3d) and S(3p) manifold and were obtained from a localized BP86 density functional theory calculation in the TZP-DKH basis with a spin-free X2C Hamiltonian to include scalar relativistic effects. We worked in the $S_z = 0$ sector with $(N_\alpha, N_\beta) = (15, 15)$ and targeted the singlet sector ($S^2 = 0$) in the projected diagonalizations. The one- and two-electron integrals were taken from the data release [48] accompanying Ref. [26]. We reported energies using the same Hamiltonian convention as Ref. [26].

Quantum circuit and released measurement dataset.

We did not perform any new quantum sampling for the [2Fe–2S] benchmark. Instead, we reused the fixed computational-basis measurement dataset [48] released with Ref. [26], and fed the identical empirical sample distribution to both SQD and CSQD. The released samples were obtained by executing a truncated LUCJ circuit [53] on an IBM Heron processor (`ibm_torino`). The circuit parameters were obtained from a restricted closed-shell CCSD calculation without additional parameter optimization. The 20-orbital active space was encoded under the Jordan–Wigner transformation on 40 qubits, while the hardware implementation used 45 qubits, 40 Jordan–Wigner qubits plus 5 auxiliary routing qubits on the heavy-hex connectivity (see Fig. 4b). This [2Fe–2S] circuit contains 1,100 two-qubit gates. The released dataset contains $|\tilde{\mathcal{X}}| = 2.4576 \times 10^6$ accepted measurement outcomes for this circuit.

Mitigation and preprocessing.

The released dataset [48] incorporated the experimental mitigation stack of Ref. [26], including twirled readout error mitigation (ROEM) [59] and dynamical decoupling (DD) [56], as well as a reset-mitigation. The postselected outcomes were used to form the empirical sample distribution that served as the common input to SQD and CSQD.

SQD and CSQD settings.

Unless otherwise stated, we used the same SQD/CSQD hyperparameters as in the N_2 benchmark. For both SQD and CSQD, we used $B = 10$ independent batches per iteration and swept $d_{\max} \in \{1000, 1500, 2000\}$. To keep the effective variational dimension budget comparable throughout the recovery iterations, we set $S_{\text{full}} = S_{\text{spin}} = d_{\max}$ and capped each spin-sector pool at d_{\max} unique single-spin strings. CSQD additionally swept the clustering model (weighted BMM [41] or k -modes [39, 40]) and the number of clusters $K \in \{2, 3, 4, 5\}$. Because the released [2Fe–2S] sample set was sufficiently large that the postselected pools already saturated d_{\max} at $t = 1$, we ran both SQD and CSQD for at most $T = 10$ self-consistent iterations. All classical post-processing for this benchmark was performed as single-node jobs using 64 CPU cores on an AMD EPYC 9755 system with 1 TB RAM.

4.5 Software and computational environment

Quantum circuit construction, compilation, and execution were performed using Qiskit 2.2.3 and qiskit-ibm-runtime 0.44.0 [60]. SQD post-processing used qiskit-addon-sqd 0.12.0 [58]. Classical electronic-structure calculations and projected diagonalizations used PySCF 2.11.0 [51, 52]. For clustering in CSQD, BMM used `stepmix` 2.2.3 [42], and k -modes used the `kmodes` library 0.12.2 [40].

Data availability. All data supporting the findings of this study are available within the paper, its Supplementary Information, and the Zenodo repository at <https://doi.org/10.5281/zenodo.18899495>.

Code availability. The CSQD source code is available from the AIQF Chem Lab Algorithms page (<https://stalwart-cassata-0d784a.netlify.app/tags/algorithm>).

Acknowledgements. This work was supported by the National Research Foundation of Korea (NRF) grant funded by the Korean government (MSIT) (no. RS-2025-005194288) and also Institute of Information & Communications Technology Planning & Evaluation (IITP) grant funded by the Korean government (MSIT) (no. RS-2025-25464788). The authors also acknowledge the Urban Big data and AI Institute of the University of Seoul supercomputing resources (<http://ubai.uos.ac.kr>) made available for conducting the research reported in this paper.

Author contributions. B.P. and K.J. conceived the study. B.P. developed the CSQD methodology. B.P., S.K., J.S., and J.B. designed the numerical experiments and implemented the software and performed computations. B.P., S.K., J.S., J.B., D.A., and K.J. analyzed and interpreted the results. K.J. acquired funding and supervised the project. B.P. wrote the initial manuscript draft, and all authors reviewed and edited the manuscript.

Competing interests. The authors declare no competing interests.

References

- [1] Imada, M., Fujimori, A. & Tokura, Y. Metal-insulator transitions. *Rev. Mod. Phys.* **70**, 1039 (1998).
- [2] Lee, P. A., Nagaosa, N. & Wen, X.-G. Doping a Mott insulator: Physics of high-temperature superconductivity. *Rev. Mod. Phys.* **78**, 17–85 (2006).
- [3] Rajca, A. Organic diradicals and polyradicals: from spin coupling to magnetism? *Chem. Rev.* **94**, 871–893 (1994).
- [4] Abe, M. Diradicals. *Chem. Rev.* **113**, 7011–7088 (2013).
- [5] Dagotto, E. Complexity in strongly correlated electronic systems. *Science* **309**, 257–262 (2005).
- [6] Georges, A., Kotliar, G., Krauth, W. & Rozenberg, M. J. Dynamical mean-field theory of strongly correlated fermion systems and the limit of infinite dimensions. *Rev. Mod. Phys.* **68**, 13 (1996).
- [7] Park, J. W., Al-Saadon, R., MacLeod, M. K., Shiozaki, T. & Vlaisavljevich, B. Multireference electron correlation methods: Journeys along potential energy surfaces. *Chem. Rev.* **120**, 5878–5909 (2020).
- [8] Zhou, C. *et al.* Electronic structure of strongly correlated systems: recent developments in multiconfiguration pair-density functional theory and multiconfiguration nonclassical-energy functional theory. *Chem. Sci.* **13**, 7685–7706 (2022).

- [9] Chan, G. K.-L. & Sharma, S. The density matrix renormalization group in quantum chemistry. *Annu. Rev. Phys. Chem.* **62**, 465–481 (2011).
- [10] Szalay, P. G., Muller, T., Gidofalvi, G., Lischka, H. & Shepard, R. Multiconfiguration self-consistent field and multireference configuration interaction methods and applications. *Chem. Rev.* **112**, 108–181 (2012).
- [11] Lyakh, D. I., Musiał, M., Lotrich, V. F. & Bartlett, R. J. Multireference nature of chemistry: The coupled-cluster view. *Chem. Rev.* **112**, 182–243 (2012).
- [12] Cohen, A. J., Mori-Sánchez, P. & Yang, W. Insights into current limitations of density functional theory. *Science* **321**, 792–794 (2008).
- [13] Cohen, A. J., Mori-Sánchez, P. & Yang, W. Challenges for density functional theory. *Chem. Rev.* **112**, 289–320 (2012).
- [14] Vogiatzis, K. D., Ma, D., Olsen, J., Gagliardi, L. & de Jong, W. A. Pushing configuration-interaction to the limit: Towards massively parallel MCSCF calculations. *J. Chem. Phys.* **147**, 184111 (2017).
- [15] Gao, H., Imamura, S., Kasagi, A. & Yoshida, E. Distributed implementation of full configuration interaction for one trillion determinants. *J. Chem. Theory Comput.* **20**, 1185–1192 (2024).
- [16] Huron, B., Malrieu, J. & Rancurel, P. Iterative perturbation calculations of ground and excited state energies from multiconfigurational zeroth-order wavefunctions. *J. Chem. Phys.* **58**, 5745–5759 (1973).
- [17] Tubman, N. M. *et al.* Modern approaches to exact diagonalization and selected configuration interaction with the adaptive sampling CI method. *J. Chem. Theory Comput.* **16**, 2139–2159 (2020).
- [18] Holmes, A. A., Tubman, N. M. & Umrigar, C. J. Heat-bath configuration interaction: An efficient selected configuration interaction algorithm inspired by heat-bath sampling. *J. Chem. Theory Comput.* **12**, 3674–3680 (2016).
- [19] Sharma, S., Holmes, A. A., Jeanmairet, G., Alavi, A. & Umrigar, C. J. Semistochastic heat-bath configuration interaction method: Selected configuration interaction with semistochastic perturbation theory. *J. Chem. Theory Comput.* **13**, 1595–1604 (2017).
- [20] Bunge, C. F. Selected configuration interaction with truncation energy error and application to the Ne atom. *J. Chem. Phys.* **125**, 014107 (2006).
- [21] Goings, J. J., Hu, H., Yang, C. & Li, X. Reinforcement learning configuration interaction. *J. Chem. Theory Comput.* **17**, 5482–5491 (2021).
- [22] Stair, N. H. & Evangelista, F. A. Exploring Hilbert space on a budget: Novel benchmark set and performance metric for testing electronic structure methods in the regime of strong correlation. *J. Chem. Phys.* **153**, 104108 (2020).
- [23] Kanno, K. *et al.* Quantum-selected configuration interaction: Classical diagonalization of hamiltonians in subspaces selected by quantum computers. *arXiv preprint arXiv:2302.11320* (2023).
- [24] Nakagawa, Y. O., Kamoshita, M., Mizukami, W., Sudo, S. & Ohnishi, Y.-y. ADAPT-QSCI: Adaptive construction of an input state for quantum-selected configuration interaction. *J. Chem. Theory Comput.* **20**, 10817–10825 (2024).

- [25] Mikkelsen, M. & Nakagawa, Y. O. Quantum-selected configuration interaction with time-evolved state. *Phys. Rev. Res.* **7**, 043043 (2025).
- [26] Robledo-Moreno, J. *et al.* Chemistry beyond the scale of exact diagonalization on a quantum-centric supercomputer. *Sci. Adv.* **11**, eadu9991 (2025).
- [27] Shirakawa, T. *et al.* Closed-loop calculations of electronic structure on a quantum processor and a classical supercomputer at full scale. *arXiv preprint arXiv:2511.00224* (2025).
- [28] Barison, S., Robledo-Moreno, J. & Motta, M. Quantum-centric computation of molecular excited states with extended sample-based quantum diagonalization. *Quantum Sci. Technol.* **10**, 025034 (2025).
- [29] Yu, J. *et al.* Quantum-centric algorithm for sample-based Krylov diagonalization. *arXiv preprint arXiv:2501.09702* (2025).
- [30] Danilov, D., Robledo-Moreno, J., Sung, K. J., Motta, M. & Shee, J. Enhancing the accuracy and efficiency of sample-based quantum diagonalization with phaseless auxiliary-field quantum Monte Carlo. *J. Chem. Theory Comput.* **21**, 11585–11594 (2025).
- [31] Shajan, A. *et al.* Toward quantum-centric simulations of extended molecules: Sample-based quantum diagonalization enhanced with density matrix embedding theory. *J. Chem. Theory Comput.* **21**, 6801–6810 (2025).
- [32] Patra, C. *et al.* Physics-informed generative machine learning for accelerated quantum-centric supercomputing. *arXiv preprint arXiv:2512.06858* (2025).
- [33] Kaliakin, D., Shajan, A., Liang, F. & Merz, K. M., Jr. Implicit solvent sample-based quantum diagonalization. *J. Phys. Chem. B* **129**, 5788–5796 (2025).
- [34] Kaliakin, D. *et al.* Accurate quantum-centric simulations of intermolecular interactions. *Commun. Phys.* **8**, 396 (2025).
- [35] Hossain, S. M., Lee, S.-C. & Bhattacharjee, S. Quantum simulations of battery electrolytes using variational quantum eigensolver, equation-of-motion, and sample-based diagonalization methods: Active-space design, dissociation, and excited states of $LiPF_6$, $NaPF_6$, and FSI salts. *Adv. Quantum Technol.* **9**, e00871 (2026).
- [36] Preskill, J. Quantum computing in the NISQ era and beyond. *Quantum* **2**, 79 (2018).
- [37] Sharma, S., Sivalingam, K., Neese, F. & Chan, G. K.-L. Low-energy spectrum of iron–sulfur clusters directly from many-particle quantum mechanics. *Nat. Chem.* **6**, 927–933 (2014).
- [38] Jordan, P. & Wigner, E. Über das paulische äquivalenzverbot. *Z. Phys.* **47**, 631–651 (1928).
- [39] Huang, Z. Extensions to the k-means algorithm for clustering large data sets with categorical values. *Data Min. Knowl. Discov.* **2**, 283–304 (1998).
- [40] de Vos, N. J. kmodes categorical clustering library. <https://github.com/nicodv/kmodes> (2022).
- [41] Nadif, M. & Govaert, G. Clustering for binary data and mixture models—choice of the model. *Appl. Stoch. Models Data Anal.* **13**, 269–278 (1997).
- [42] Morin, S. *et al.* StepMix: A Python package for pseudo-likelihood estimation of generalized mixture models with external variables. *J. Stat. Softw.* **113**, 1–39 (2025).
- [43] Perdew, J. P. Density-functional approximation for the correlation energy of the inhomogeneous electron gas. *Phys. Rev. B* **33**, 8822 (1986).

- [44] Becke, A. D. Density-functional exchange-energy approximation with correct asymptotic behavior. *Phys. Rev. A* **38**, 3098 (1988).
- [45] Jorge, F., Canal Neto, A., Camiletti, G. & Machado, S. Contracted Gaussian basis sets for Douglas–Kroll–Hess calculations: Estimating scalar relativistic effects of some atomic and molecular properties. *J. Chem. Phys.* **130**, 064108 (2009).
- [46] Liu, W. Ideas of relativistic quantum chemistry. *Mol. Phys.* **108**, 1679–1706 (2010).
- [47] Li, Z., Xiao, Y. & Liu, W. On the spin separation of algebraic two-component relativistic hamiltonians. *J. Chem. Phys.* **137**, 154114 (2012).
- [48] jrm874. jrm874/sqd_data_repository: 0.0.1. <https://doi.org/10.5281/zenodo.15324153> (2025).
- [49] White, S. R. Density matrix formulation for quantum renormalization groups. *Phys. Rev. Lett.* **69**, 2863 (1992).
- [50] Reinholdt, P. *et al.* Critical limitations in quantum-selected configuration interaction methods. *J. Chem. Theory Comput.* **21**, 6811–6822 (2025).
- [51] Sun, Q. *et al.* Recent developments in the PySCF program package. *J. Chem. Phys.* **153**, 024109 (2020).
- [52] Sun, Q. *et al.* PySCF: the Python-based simulations of chemistry framework. *Wiley Interdiscip. Rev.-Comput. Mol. Sci.* **8**, e1340 (2018).
- [53] Motta, M., Sung, K. J., Whaley, K. B., Head-Gordon, M. & Shee, J. Bridging physical intuition and hardware efficiency for correlated electronic states: the local unitary cluster Jastrow ansatz for electronic structure. *Chem. Sci.* **14**, 11213–11227 (2023).
- [54] Matsuzawa, Y. & Kurashige, Y. Jastrow-type decomposition in quantum chemistry for low-depth quantum circuits. *J. Chem. Theory Comput.* **16**, 944–952 (2020).
- [55] The ffsim developers. ffsim: Faster simulations of fermionic quantum circuits. <https://github.com/qiskit-community/ffsim> (2025).
- [56] Viola, L. & Lloyd, S. Dynamical suppression of decoherence in two-state quantum systems. *Phys. Rev. A* **58**, 2733 (1998).
- [57] Van Den Berg, E., Mineev, Z. K. & Temme, K. Model-free readout-error mitigation for quantum expectation values. *Phys. Rev. A* **105**, 032620 (2022).
- [58] Saki, A. A. *et al.* Qiskit addon: sample-based quantum diagonalization. <https://github.com/Qiskit/qiskit-addon-sqd> (2024).
- [59] Nation, P. D., Kang, H., Sundaresan, N. & Gambetta, J. M. Scalable mitigation of measurement errors on quantum computers. *PRX Quantum* **2**, 040326 (2021).
- [60] Javadi-Abhari, A. *et al.* Quantum computing with Qiskit. *arXiv preprint arXiv:2405.08810* (2024).